AIMS Materials Science, 13(2): 258–281.
DOI: 10.3934/matersci.2026015
Received: 20 December 2025
Revised: 22 February 2026
Accepted: 11 March 2026
Published: 23 March 2026

https://www.aimspress.com/journal/Materials

Research article

First-principles calculations and experiments of AgAu and microalloyed AgAu systems

Lisen Huang[1], Kun Zhu[2], Jianying Yang[3], Junjie Feng[2], Hui Xiong[1], Rong Jiang[1] and Xiaolong Zhou[1,*]

[1] Faculty of Materials Science and Engineering/Key Laboratory of Advanced Materials of Yunnan Province, Kunming University of Science and Technology, Kunming 650093, China
[2] School of Physics and Electrical Engineering, Liupanshui Normal University, Liupanshui 553000, China
[3] Panzhihua University, Panzhihua 617000, China

* **Correspondence:** Email: kmzxlong@163.com.

Abstract: Microalloying elements (<1 wt%) are widely used in the steel industry, but their effect on AgAu alloys is still unclear. Therefore, this paper uses first-principles calculations and experimental verification to explore this topic. For first-principles calculations, the formation enthalpy, elastic constants, and mechanical properties of AgAu alloys and microalloyed AgAu systems (doped with Pd, Pt, Ni, Cu, Zn, Ti, Y, Be, Mg, Al, Sr) were calculated. The results show that the AgAu alloys and AgAu-M alloys have thermodynamic and mechanical stability. Doping elements increase the hardness, shear modulus, and Young's modulus of the alloys to varying degrees. Except for Be, other doping elements all reduce the elastic anisotropy index of the alloys to varying degrees. Experimentally, an Ag-16wt%Au-0.5wt%Al alloy was prepared, and the alloy contained Ag, Au, AlAu, and trace amounts of $AlAu_2$ phases. The experimental hardness value was slightly lower than the calculated value. Energy-dispersive spectrometer (EDS) results proved that the alloy matrix was an Ag(Au, Al) solid solution and the intermetallic phase AlAu was distributed in the matrix. Additionally, trace amounts of the $AlAu_2$ may be interspersed within the Ag(Au, Al) solid solution. There is a certain mutual verification between the calculation results and experimental results in this article. Therefore, this study provides a new approach to improving the performance of AgAu alloys by doping with microalloying elements.

Keywords: first-principles calculations; microalloying elements; mechanical properties; electronic properties

1. Introduction

As a naturally good conductor, the precious metal silver is widely utilized in various fields, including bonding wires [1], electrodes [2], high-performance printed circuit boards [3], and conductive probes for microstructure inspection equipment [4]. This widespread use is attributed to its exceptional electrical and thermal conductivity, as well as its high ductility. However, the inherent softness of pure silver, combined with its susceptibility to react with sulfides in humid environments, raises concerns regarding its mechanical properties and corrosion resistance [5]. In order to improve these problems, alloying elements are added to the silver matrix to adjust the overall mechanical properties of the alloy, and at the same time, silver can be passivated to improve corrosion resistance. Elements suitable for alloying with silver include Au, Pt, Pd, Ru, etc. Bacon et al. [6] measured the elastic constants of Ag, as well as Ag-3.07Mg, Ag-2.4Zn, Ag-6.22Pd, Ag-3.17Sn, and Ag-8.63In dilute solid solutions (at%), by ultrasonic pulse echo method. It was found that the trace element Pd improves the bulk modulus of the Ag, while the Mg, Zn, Sn, and In elements decreased the bulk modulus of Ag to different degrees, with a greater decrease in the shear constant $(C_{11}–C_{12})/2$. Kuo et al. [7] doped Ag-3 wt% Pd matrix with 8, 15, 20, and 28 wt% Au. It was found that the Vickers hardness increased from 1.46 to 2.59 GPa and the elasticity modulus increased from 43.02 to 78.01 GPa with increasing Au doping. On the contrary, their elongation and conductivity are very low, which is caused by the high content of Au and the low angular grain boundary density that enhances the electron scattering [8]. Tseng et al. [9] examined the influence of Pd addition on the mechanical and electrical properties of silver bonding wires. The results showed that Pd-doped silver wires exhibit a shorter heat-affected zone after annealing compared to conventional silver wires, along with superior mechanical performance. During bonding with aluminum pads, intermetallic compounds, such as Ag_3(Pd)Al and Ag(Pd)Al, were formed, and the formation of these phases significantly enhanced the bonding stability. In addition, the doping of elements, such as Au and Pd, in the Ag matrix improves the corrosion and oxidation resistance of the alloys by reducing the surface activity of the metal. Therefore, effective regulation of the content of doping elements, such as Au, is a recipe for optimizing the mechanical and electrical properties of silver alloys.

Experimental studies of silver-gold alloys have been greatly limited by the high price of precious metals, such as Ag, Au, Pt, and Pd. The first-principles computational approach is widely used to simulate and calculate crystal structures, leading to theoretical explorations of material properties, such as structural stability, mechanical and electrical properties, catalysis, and adsorption. It is particularly suitable for simulating and calculating precious and transition metal alloys [10–13]. Gong [14] calculated the silver-gold alloy clusters throughout the entire composition range and found that as the Au content increased, the bulk modulus showed a linear increase trend. Taking $Ag_{50}Au_{50}$ as an example, he studied the effect of alloy and mechanical mixture on the electronic structure and found that the AgAu interaction had little effect on the electronic structure and could be ignored. Han et al. [15] replaced Ag and Au atoms in doped silver-gold alloys with Al; constructed structural models with different Al contents; and investigated the stability, mechanical properties, and electronic structure of

Ag-Au-Al ternary alloys, and their calculated results were in good agreement with experimental results. Yi et al. [16] investigated the effects of various alloying elements, including Sn, In, Zn, Cu, Zr, Ni, Ir, Cr, and W, on the point defect formation enthalpy and generalized stacking fault energy (GSFE) of Ag-based alloys. The calculated results indicate that the ability of these alloying elements to form point defects follows the order: Sn > In > Zn > Cu > Zr > Ni > Ir > Cr > W.

Therefore, in this paper, the crystal structure, stability, mechanical properties, and electronic structure of AgAu alloys are calculated using first-principles. The optimal silver-gold alloys are doped with microalloying elements by the virtual crystal approximation (VCA) method [17,18] to calculate the mechanical properties and electronic structures of the alloys and to compare the effects of different microalloying elements on these two aspects of the silver-gold matrix. In the field of ab initio first-principles calculations, VCA is popular for dealing with disordered alloys, and calculations of elastic constants for alloys are considered to be accurate. In particular, since the doping of microalloying elements tends to be very low (less than 1 wt%), it is not possible for this series of alloys to form disordered alloys similar to high-entropy alloys. In constructing the model, both Ag and Au belong to the face-centered cubic structure of the Fm-3m [225] space group, with three face-cantered atoms and one top corner atom constituting a unit cell, and the AgAu alloy is an infinite solid solution, a 2 × 2 × 2 Ag supercell was built, and doped to form the $Ag_{32-x}Au_x$ (x = 1, 2, 3, 4, 5, 6, 7, 8) alloy [19]. Based on the $Ag_{29}Au_3$ alloy, microalloying elements (Pd, Pt, Ni, Cu, Zn, Ti, Y, Be, Mg, Al, Sr) were added to the central Ag site by the VCA method in order to avoid the alloying disorder being too high, which may cause a great deviation from the actual situation. All elements are doped at 0.5 wt% except Be which is doped at 0.25 wt%.

2. Methods and methods

2.1. Calculation details

All calculations in this article were performed using the Cambridge Sequential Total Energy Package (CASTEP) program based on density functional theory (DFT) [20]. CASTEP is an advanced quantum mechanics computational program based on DFT, which can accurately simulate the crystal structure and surface properties of various solid-state materials such as semiconductors, ceramics, metals, minerals, etc., to achieve in-depth analysis of their properties [21]. The exchange correlation function used in the alloy calculations is the Perdew-Burke-Ernzerhof (PBE) function under the generalized gradient approximation (GGA), which is used to deal with exchange correlations between electron gases [22]. The on-the-fly generated ultrasoft pseudopotential (OTFG USPP) is also used [23]. The total energy is calculated using a self-consistent iterative method, where the density mixing method is the Pulay method [24]. Prior to the energy and various property calculations, a geometry optimization was carried out using the BFGS (Broyden-Flecher-Goldfarb-Shanno) algorithm to allow the atoms and cells to relax freely so that the ground state energies of the system could be obtained [25]. Finite basis set corrections were used for the total energy calculations. Convergence test calculations for the truncation energy and k-point density were performed with the aim of ensuring that the model structure can be calculated with a high degree of accuracy and possesses a not-so-low degree of confidence given the available computational resources and computer configurations. The results of the convergence test determined that the truncation energy parameter was set to 540 eV and the k-point network was set to 6 × 6 × 6. The threshold parameters for the geometrical structure relaxation were set as follows: the Self-Consistent Field (SCF) converged at 1×10^{-6} eV/atom, the

energy converged at 1×10^{-5} eV/atom, the maximum stress was 0.03 eV/Å, the maximum internal pressure was 0.05 GPa, the maximum displacements of the atoms were limited to the range of 0.001 Å.

2.2. Experiment

In this study, we conducted experiments using an AgAu-Al alloy as a model system. An Ag-16wt%Au-0.5wt% Al(Ag-9.375at%Au-2.15at%Al) alloy sample was prepared to validate the calculated results. The experimental procedure was as follows: Ag, Au, and Al were pre-treated to a clean state. Then, 8.35 g of Ag, 1.6 g of Au, and 0.05 g of Al were weighed and placed in a GP30-CW7 vacuum arc melting furnace. The furnace was evacuated to 5×10^{-2} GPa, filled with an argon atmosphere, and then heated to 1100 ℃. After the metal melted, it was held for 5 min, and then heating was stopped and it was cooled. Afterwards, the alloy was annealed in a SK2-4-12TPB3 vacuum tube furnace, and the furnace was washed with argon before annealing. The annealing temperature was set to 500 ℃ and held for 48 h, ensuring that the furnace was in a vacuum state during the annealing process.

Phase analysis of the alloy samples was conducted using X-ray diffraction (XRD-MiniFlex600, Cu target, Kα = 1.5406 Å, 40 kV, 50 mA, with a scanning speed of 5 °/min). Morphological analysis and compositional characterization were performed using a scanning electron microscope (SEM, Tecnai G2 TF30) equipped with an energy-dispersive spectrometer (EDS). Hardness tests on the samples were carried out using an HMVG-FA automatic micro-Vickers hardness tester.

3. Results and discussion

3.1. Calculation of $Ag_{32-x}Au_x$

3.1.1. Crystal structure and stability analysis of $Ag_{32-x}Au_x$ alloy

The calculated lattice constant of the Ag unit cell is 4.202 Å, which is about 2.7% higher than the experimental result in the literature (4.09 Å) [26], which is due to the inherent problem of overestimation of lattice constants in the GGA function. The crystal structure of the silver-gold alloy $Ag_{32-x}Au_x$ (x = 1, 2, 3, 4, 5) is shown in Figure 1. When Au is doped into the silver matrix, the lattice parameters of the relaxation structure model change due to the influence of the electron shells and nuclei as well as the interactions between the silver and gold atoms, despite the fact that the metallic radii r_{met} of the silver and gold atoms are approximately the same (Ag: 1.4445 Å, Au: 1.442 Å) [27]. Figure 2 shows the variation of lattice parameters of $Ag_{32-x}Au_x$, which gradually decreases with the increase of Au atoms, but the magnitude of the change is not significant. The alteration between the two crystal structures is minimal, with a difference of only 0.32%. Furthermore, the discrepancy between $Ag_{32}Au_1$ and $Ag_{27}Au_5$ is 0.4%. Since the lattice constant of Au is slightly smaller than that of Ag, it is reasonable to expect that an increase in Au content would result in a slight decrease in the lattice parameter.

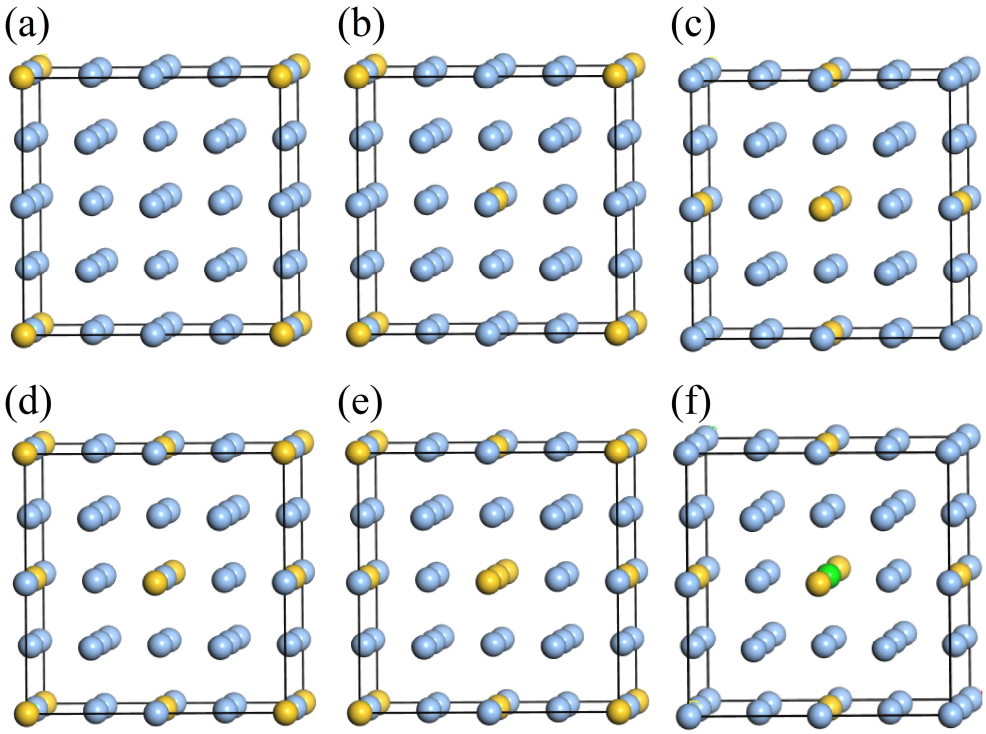

Figure 1. Crystal structure. (a–e) $Ag_{32-x}Au_x$ (x = 1, 2, 3, 4, 5). (f) AgAu-M (M = Pd, Pt, Ni, Cu, Zn, Ti, Y, Be, Mg, Al, Sr). (The yellow, blue, and green spheres represent Ag, Au, and mixed atoms, respectively).

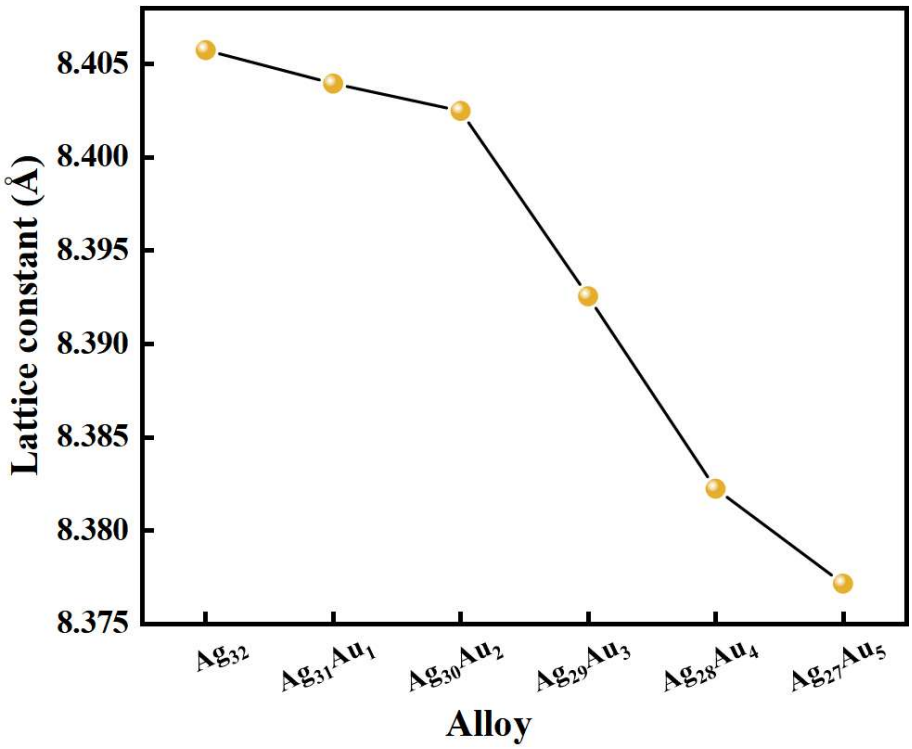

Figure 2. Lattice parameters of $Ag_{32-x}Au_x$ (x = 1, 2, 3, 4, 5) alloy.

The formation enthalpy (ΔH) and binding energy (E_{coh}) can be used as thermodynamic criteria to determine the stability of AgAu alloys. Combining can describe the energy required to connect two or more isolated parts into a stable structure in a system. Usually, a crystal structure with lower binding energy means it has higher stability. The value of enthalpy of formation can reflect the feasibility and difficulty of a substance's reaction. Specifically, when the enthalpy of formation is negative and the value is smaller, it indicates that the reaction is more likely to occur. The formation enthalpy and binding energy of $Ag_{32-x}Au_x$ are calculated, respectively, by the following Eqs 1 and 2 [28]:

$$\Delta H = \frac{E_{total} - xE_{solid}(X) - yE_{solid}(Y)}{x+y} \tag{1}$$

$$E_{coh} = \frac{E_{total} - xE_{atom}(X) - yE_{atom}(Y)}{x+y} \tag{2}$$

In the equations, E_{total}, $E_{solid}(X)$, and $E_{atom}(X)$ represent the total energy of the alloy and the energy of the X atom in the solid system and isolated system, respectively. x and y represent the number of corresponding atoms X and Y in the structural model. The formation enthalpy and binding energy of each model after structural optimization were listed in Table 1. As can be seen from Table 1, the formation enthalpy of all the $Ag_{32-x}Au_x$ alloys is negative, indicating that all the structures are thermodynamically stable, and the $Ag_{29}Au_3$ alloy has the smallest formation enthalpy of –0.139 eV, indicating that it has the strongest formation ability of all the alloys, and is the first to form under the same conditions. Next are $Ag_{30}Au_2$ and $Ag_{31}Au_1$ alloys. The data of binding energy is also negative, indicating that the Ag and Au atoms of these structures can overcome atomic repulsive force and bind together to form a stable structure. The more negative the value, the stronger their binding ability. The data show that $Ag_{24}Au_8$ alloy has the smallest binding energy of –3.000 eV/atom, but the formation enthalpy of this alloy is relatively high. This is followed by the $Ag_{29}Au_3$ alloy, which, in combination with the data on the formation enthalpy, suggests that the stability of this alloy is so superior that it deserves further in-depth study.

Table 1. Formation enthalpy and binding energy of $Ag_{32-x}Au_x$ (x = 1, 2, 3, 4, 5) alloy.

Alloy	Formation enthalpy (eV/atom)	Binding energy (eV/atom)
$Ag_{31}Au_1$	–0.134	–2.966
$Ag_{30}Au_2$	–0.137	–2.981
$Ag_{29}Au_3$	–0.139	–2.995
$Ag_{28}Au_4$	–0.063	–2.930
$Ag_{27}Au_5$	–0.068	–2.948

3.1.2. Mechanical properties of $Ag_{32-x}Au_x$ alloy

In order to reveal the mechanical properties of $Ag_{32-x}Au_x$ alloys, the elastic constants of each alloy structure are calculated in this paper, and the results are listed in Table 2. Since all the $Ag_{32-x}Au_x$ structures are cubic, their elastic constants should satisfy the mechanical stability criterion, namely the Born criterion (Eq 3) [29]:

$$C_{11} > 0, C_{12} > 0, C_{44}, C_{11} > |C_{12}|, C_{11} + 2C_{12} > 0 \tag{3}$$

By substituting the data from Table 2 into the judgment criteria, it was found that the $Ag_{32-x}Au_x$ (x = 1, 2, 3, 4, 5) alloy structure meets the criteria and exhibits mechanical stability.

Table 2. Elastic constants (C_{ij}) of $Ag_{32-x}Au_x$ (x = 1, 2, 3, 4, 5) alloy.

Alloy	C_{11} (GPa)	C_{12} (GPa)	C_{44} (GPa)
$Ag_{31}Au_1$	68.42	49.54	24.96
$Ag_{30}Au_2$	68.76	52.20	23.43
$Ag_{29}Au_3$	75.67	58.16	30.57
$Ag_{28}Au_4$	80.93	63.22	29.60
$Ag_{27}Au_5$	85.35	65.91	34.30

The elastic modulus of the alloy can be calculated through the elastic constant and related formulas, and these different elastic moduli can reflect the mechanical properties of the material. According to the Voigt (V)-Reuss (R)-Hill (H) model [28–30], bulk modulus (B) and shear modulus (G) can be calculated. In addition, the Young's modulus (E) can also be calculated from formulas containing B and G. The formulas for calculating the cubic crystal system are as Eqs 4 and 5:

$$\begin{cases} B_V = B_R = \frac{C_{11}+2C_{12}}{3} \\ G_V = \frac{(C_{11}-C_{12}+3C_{44})}{5} \\ G_R = \frac{5C_{44}(C_{11}-C_{12})}{4C_{44}+3(C_{11}-C_{12})} \end{cases} \tag{4}$$

$$\begin{cases} B = B_H = \frac{B_V+B_R}{2} \\ G = G_H = \frac{G_V+B_R}{2} \end{cases} \tag{5}$$

Young's modulus (E) can be calculated from B and G (Eq 6) [31]:

$$E = \frac{9BG}{3B+G} \tag{6}$$

After calculation, the elastic modulus was obtained (Table 3). In order to display the magnitude of elastic moduli more intuitively, this article drew a bar chart of elastic modulus, as shown in Figure 3. The resistance of materials to deformation can be measured by bulk modulus and shear modulus, where bulk modulus refers to the response of an elastic body when subjected to pressure (bulk stress) and shear modulus refers to the response of an elastic body when subjected to tangential force (shear stress) [32]. From Figure 3a, it can be seen that as the Au content increases, B also increases. The $Ag_{27}Au_5$ alloy has the largest bulk modulus, indicating that its ability to resist external pressure is the strongest, and its deformation degree is the smallest under the same external pressure. In terms of shear modulus and Young's modulus, both B and E show a gradually increasing trend, and the change is consistent with C_{44}. The addition of Au significantly improves the modulus of pure Ag, which can effectively enhance the resistance of Ag to external stress.

The Poisson's ratio (ν) and B/G derived from the elastic modulus can reflect the toughness and ductility of the material. The formula for calculating Poisson's ratio is as Eq 7 [31]:

$$v = \frac{3B-2G}{2(3B+C)} \tag{7}$$

Figure 3b shows the Poisson's ratio and B/G of the $Ag_{32-x}Au_x$ alloy material. The value of Poisson's ratio ranges from 0.362 to 0.378, while the range of B/G values is from 3.302 to 3.779, and the trends of the two changes are consistent. The various structures of $Ag_{32-x}Au_x$ alloy are higher than the standard value of toughness, showing toughness and ductility, which indirectly indicates that $Ag_{32-x}Au_x$ alloy material has good machinability [33,34]. Arrange Poisson's ratio and B/G in descending order: $Ag_{28}Au_4$ > $Ag_{30}Au_2$ > $Ag_{27}Au_5$ > $Ag_{29}Au_3$ > $Ag_{31}Au_1$.

At present, there are many articles on using elastic modulus and Poisson's ratio to calculate the theoretical hardness of materials, all of which have their own corresponding scope and requirements [33–35]. In this paper, the Vickers hardness formula proposed by Tian in 2012 is used to calculate the corresponding Vickers hardness (*Hv*) of alloys by combining the bulk modulus and shear modulus obtained earlier (Eq 8) [34]:

$$Hv = 0.92\left(\frac{G}{B}\right)^{1.137} G^{0.708} \tag{8}$$

The Debye temperature coefficient (θ_D) can be used to determine the strength of chemical bonds within solid materials. The Debye temperature coefficient can be calculated using Eq 9 [36,37]:

$$\begin{cases} v_t = \left(\frac{\mathrm{G}}{\rho}\right)^{\frac{1}{2}} \\ v_l = \left(\frac{B+\frac{3}{4}G}{\rho}\right)^{\frac{1}{2}} \\ v_m = \left[\frac{1}{3}\left(\frac{1}{v_t^3}+\frac{2}{v_l^3}\right)\right]^{-\frac{1}{3}} \\ \theta_{\mathrm{D}} = \frac{h}{k}\left[\frac{3\mathrm{n}}{4\pi}\left(\frac{\mathrm{N_A}\rho}{\mathrm{m}}\right)\right]^{\frac{1}{3}} v_m \end{cases} \tag{9}$$

where h is the Planck constant; k is the Boltzmann constant; n is the number of atoms; N_A is the Avogadro number; m is the atomic mass; ρ is the material density; v_t and v_l are the transverse sound velocities and longitudinal sound velocities, respectively; and v_m is the average sound velocity. Figure 3c shows the Vickers hardness and Debye temperature coefficient of $Ag_{32-x}Au_x$ alloy. It is evident that the Vickers hardness and Debye temperature coefficient have a consistent trend, and the Debye temperature coefficient also reflects the hardness relationship of the alloy material. The hardness value of $Ag_{27}Au_5$ alloy is the highest, while the hardness value of $Ag_{30}Au_2$ alloy is the lowest. Although $Ag_{27}Au_5$ alloy has the highest hardness among all structures, the Poisson's ratio and B/G data in Figure 3b still indicate that the alloy material has good toughness and ductility, making it a very worthwhile alloy composition to study in this series of alloys.

The elastic anisotropy index (A^U) is one of the key mechanical properties of materials. The elastic anisotropy index can be described by A^U (Eq 10) [38,39]:

$$A^U = 5\frac{G_V}{G_R} + \frac{B_V}{B_R} - 6 \tag{10}$$

When the elastic anisotropy index A^U value is 0, it indicates that the material is isotropic, otherwise the material exhibits anisotropy. The degree of material anisotropy is represented by the degree of deviation of the A^U value from 0. Figure 3d illustrates the elastic anisotropy index of the $Ag_{32-x}Au_x$ alloy, demonstrating that all alloys display elastic anisotropy. The alloy $Ag_{27}Au_5$ exhibits the highest A^U value, followed by $Ag_{29}Au_3$. The elastic anisotropy index provides only a rough representation of the degree of material anisotropy. To facilitate intuitive analysis of elastic anisotropy, this article also plots the three-dimensional diagram of Young's modulus (Figure 4) based on the flexibility coefficient S_{ij}. Here, a high value, represented by the color red, means a high resistance to external forces in that direction, and a low value, represented by the color blue, means a weak resistance to external forces in that direction. When the A^U value is 0, the three-dimensional space map of Young's modulus should be a smooth sphere. It can be seen that the $Ag_{27}Au_5$ alloy deviates the most from the spherical shape, and there may be many microcracks inside the alloy material. The tip effect of microcracks often reduces the yield strength and hardness of materials, leading to a significant decrease in the mechanical properties of alloys [40]. $Ag_{31}Au_1$ alloy has the smallest deviation from spherical shape because its elastic anisotropy index is also the smallest. It is obvious that all alloy structures have very low values in the [001], [010], and [100] directions, indicating that stiffness in these directions is very small and their resistance to external deformation is weak. The magnitude of the three-dimensional diagram of Young's modulus scale numbers is also consistent with the trend of Young's modulus (E) in Figure 3a. Overall, the incorporation of Au leads to a continuous increase in A^U of the AgAu alloy.

Table 3. Mechanical properties of $Ag_{32-x}Au_x$ (x = 1, 2, 3, 4, 5) alloy.

Alloy	B (GPa)	G (GPa)	E (GPa)	v	B/G	Hv (GPa)	θ_D (K)	A^U
$Ag_{31}Au_1$	55.83	16.91	46.07	0.362	3.302	1.751	163.31	1.23
$Ag_{30}Au_2$	57.72	15.45	42.55	0.377	3.736	1.428	154.29	1.42
$Ag_{29}Au_3$	64.00	18.58	50.82	0.368	3.444	1.785	165.59	2.13
$Ag_{28}Au_4$	69.12	18.29	50.43	0.378	3.779	1.589	162.92	1.97
$Ag_{27}Au_5$	72.39	20.76	56.84	0.369	3.487	1.904	179.52	2.17

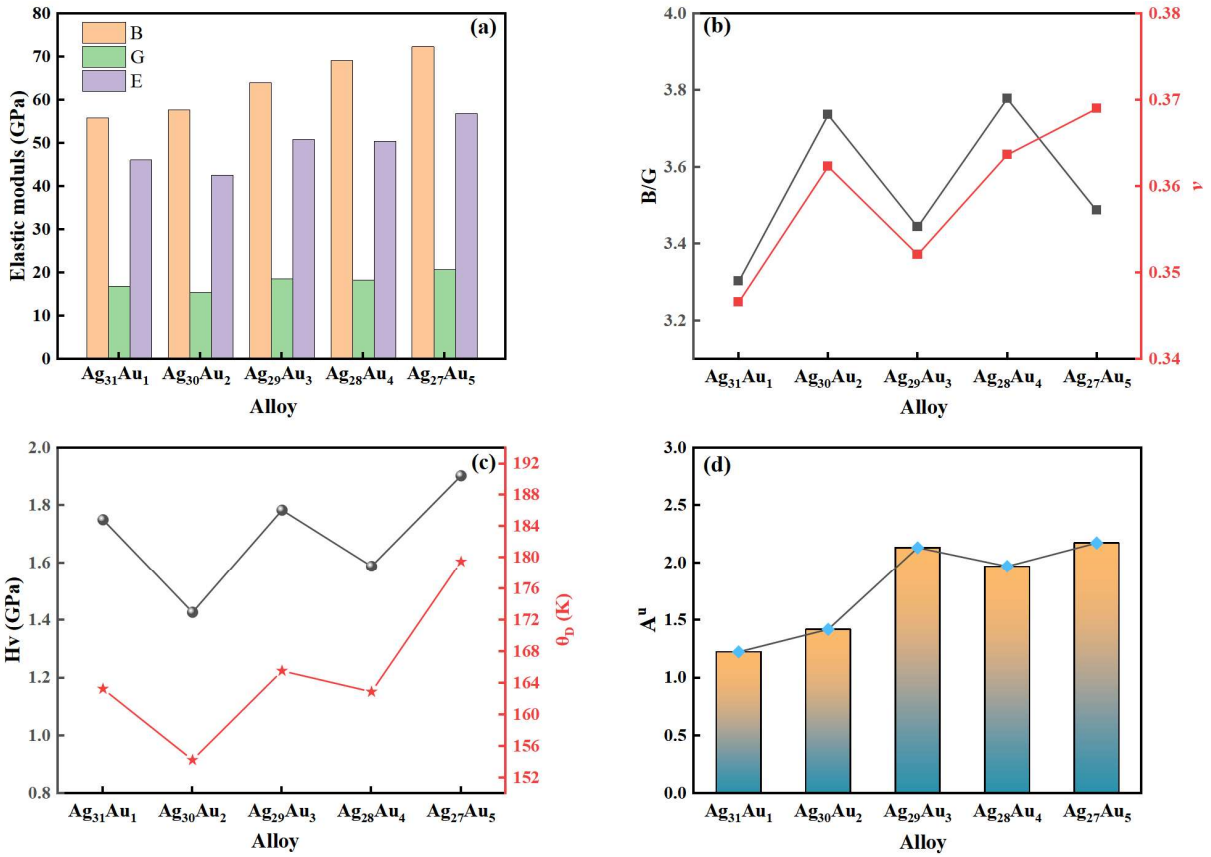

Figure 3. Mechanical properties of $Ag_{32-x}Au_x$ (x = 1, 2, 3, 4, 5) alloy: (a) elastic modulus; (b) B/G and *v*; (c) *Hv*; and (d) A^U.

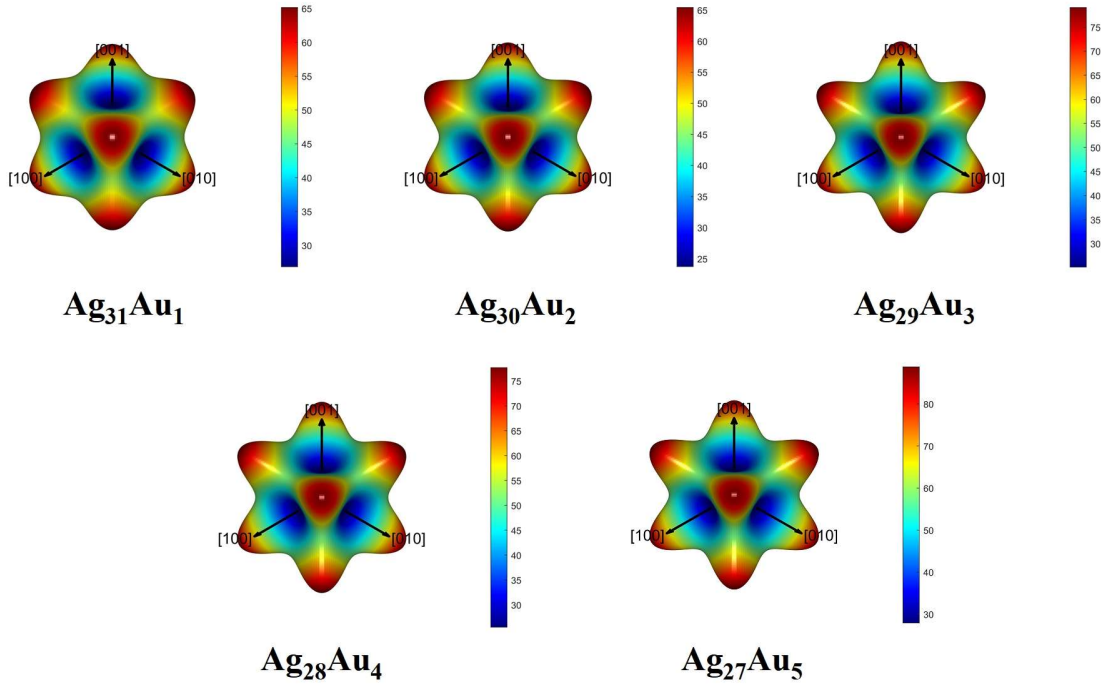

Figure 4. Three-dimensional diagram of Young's modulus of $Ag_{32-x}Au_x$ (x = 1, 2, 3, 4, 5) alloy.

3.1.3. Electronic properties of $Ag_{32-x}Au_x$ alloy

The performance of materials is closely related to electronic structure. The electronic structure determines the lattice stability, mechanical, and electrical properties of materials by influencing factors, such as energy band structure, electron density, and chemical bonding types. Understanding the relationship between electronic structure and material properties is of great importance for the design and application of materials [41]. In order to analyze the electronic structure of the $Ag_{32-x}Au_x$ alloy in its ground state and to study the nature of the bonding between the atoms of the $Ag_{32-x}Au_x$ alloy, the density of states of the alloy, including the total density of states (TDOS) and the partial density of states (PDOS), were calculated in this paper, as shown in Figure 5.

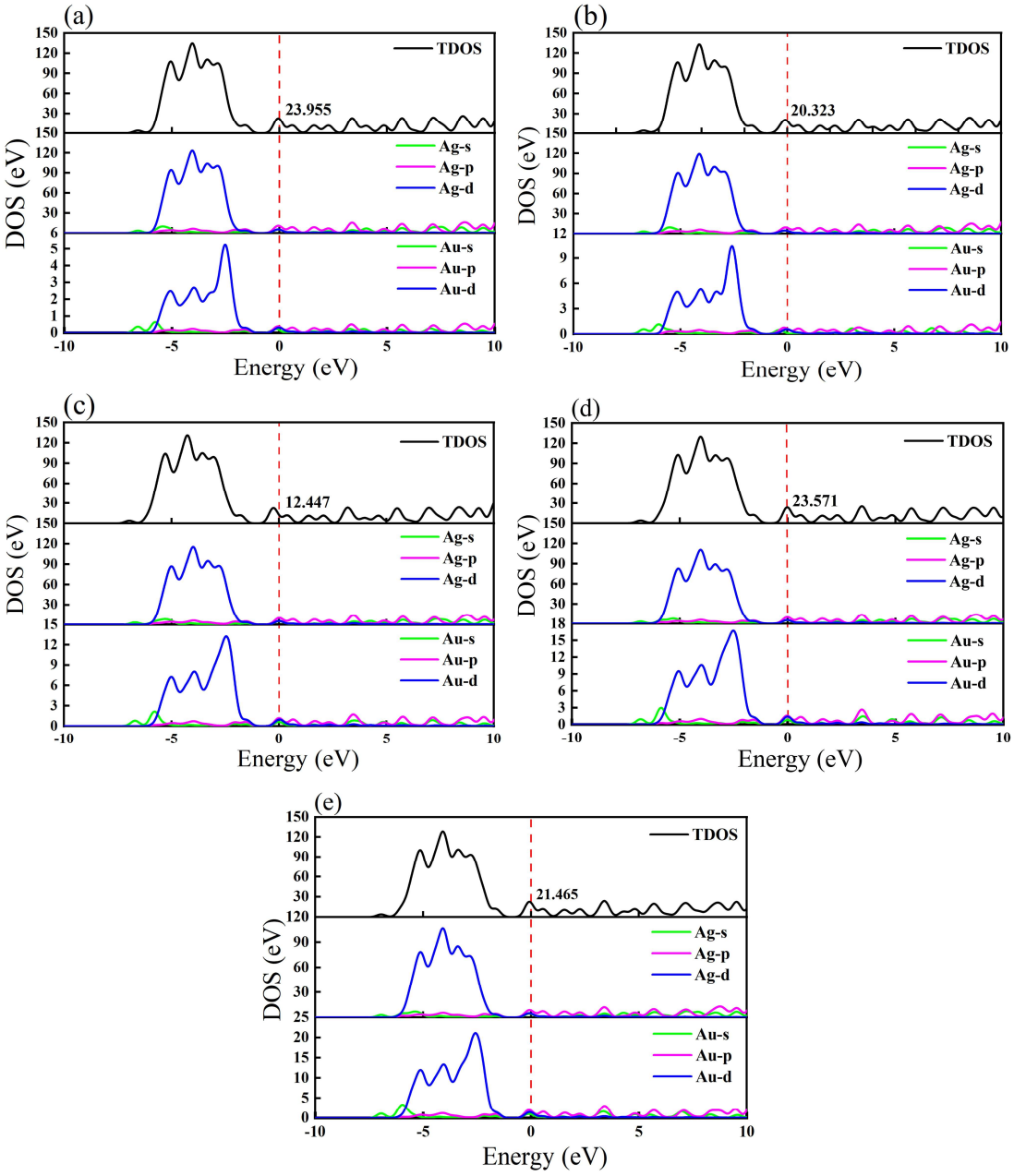

Figure 5. Total density of states and partial density of states of $Ag_{32-x}Au_x$ (x = 1, 2, 3, 4, 5) alloy.

The energy at 0 in each figure is the Fermi energy level (E_f), indicated by the red dotted line The presence of a certain density of electronic states at this point suggests a likelihood of being filled with electrons at E_f, thereby indicating that the material exhibits metallic properties and is classified as a metallic material. The TDOS at E_f is contributed by the p-orbitals and d-orbitals of Ag and Au atoms. At the same time, the lower the value of the density of states there, the stronger the bonding strength and the more stable the alloy, which tends to exhibit better properties. The total density of states of $Ag_{29}Au_3$ alloy is the lowest at the E_f (Figure 5c, 12.447 eV), which is consistent with the previous analysis that $Ag_{29}Au_3$ alloy has the lowest formation enthalpy, lower binding energy, and highest hardness. As the Au content continues to increase, the change in total density of states is not very significant, but the contribution of Ag d-orbitals to TDOS becomes smaller and smaller, while the contribution of Au d-orbitals to TDOS becomes larger and larger, which conforms to the general rule. Overall, the d-orbitals of Ag and Au contribute the most to the density of states in the −7~−2 eV energy range, much higher than the s-orbitals and p-orbitals. Therefore, the p-orbitals of both form larger hybridization peaks. Several small peaks between the energy range of 1~6 eV are formed by the hybridization of Ag p-orbitals with Au s and p-orbitals. Due to the low energy level, which is unrelated to the gain or loss of electrons, it will not be discussed here.

3.2. The influence of microalloying elements on $Ag_{29}Au_3$ alloy

The doping sites in the AgAu model can be broadly categorized into Ag atomic sites and Au atomic sites. When different elements are doped at the central Ag site versus the face-centered Au site, the calculated formation enthalpies (Table 4) reveal that the formation enthalpy is lower when the dopant forms a mixed atom with the central Ag atom compared to doping at the face-centered Au site. Therefore, we selected the central Ag site for doping with various elements to construct the VCA model.

Table 4. Formation enthalpy of elements at different sites.

Elements	Ag site △H (eV/atom)	Au site △H (eV/atom)
Pd	–0.1377	–0.1094
Pt	–0.2648	–0.1260
Sr	–0.0952	–0.0771
Ti	–0.1145	0.0988
Y	–0.1103	–0.4307
Zn	–0.1752	0.1219
Be	–0.1242	–0.0292
Cu	–0.1835	–0.2964
Mg	–0.1562	0.1210
Al	–0.1606	–0.1289
Ni	–0.1745	–0.4406

3.2.1. Crystal structure and stability analysis of AgAu-M alloy

Based on the previous analysis, this article has conducted a more in-depth study on $Ag_{29}Au_3$ alloy in order to obtain better mechanical properties. On the basis of the $Ag_{29}Au_3$ alloy, VCA method was used to add microalloying elements (Pd, Pt, Ni, Cu, Zn, Ti, Y, Be, Mg, Al, Sr) at the center of the structure on the Ag atoms (Figure 1f). The doping content of all elements is 0.5 wt%. Since the VCA method generates virtual mixed atoms, it is not appropriate to measure the system stability using the energy standards of pure elements. Eq 1 is no longer applicable to structures containing mixed atoms. The central atom of this structure is a mixture of silver and microalloying elements, forming a complete crystal structure together with the remaining 28 Ag atoms and 3 Au atoms. Therefore, Eq 1 can be rewritten as Eq 11 [42,43]:

$$\Delta H = \frac{E_{total} - 28E_{solid}(Ag) - 3E_{solid}(Au) + E_{solid}(Mixed\ atom)}{32} \tag{11}$$

where E_{total} is the total energy of the alloy, $E_{solid}(Ag)$ and $E_{solid}(Au)$ are the single atomic energy of Ag and Au atoms in the solid system, and $E_{solid}(Mixed\ atom)$ is the single atomic energy of mixed atoms in the solid system, which can be calculated by the VCA method.

The single atomic energies of Ag and Au are –4006.072 and –14128.943 eV, respectively. The formation enthalpy data of AgAu-M alloys was calculated using Eq 11 and listed in Table 5. From the Table 4, it can be seen that the formation enthalpy of all alloys is negative and thermodynamically stable, indicating that stable structures can still be formed after doping trace elements into AgAu alloys. The formation enthalpy of AgAu-Pt is the smallest, while the formation energy of AgAu-Sr is the largest.

Table 5. Formation enthalpy of AgAu-M alloy.

Alloy	E_{total} (eV/atom)	$E_{solid}(Mixed\ atom)$ (eV/atom)	Formation enthalpy (eV/atom)
AgAu-Pd	–158474.703	–3913.446	–0.1377
AgAu-Pt	–161121.958	–6556.634	–0.2648
AgAu-Sr	–157641.192	–3081.294	–0.0952
AgAu-Ti	–157634.322	–3073.807	–0.1145
AgAu-Y	–157738.158	–3177.776	–0.1103
AgAu-Zn	–158340.066	–3777.610	–0.1752
AgAu-Be	–154952.354	–391.529	–0.1242
AgAu-Cu	–158178.044	–3615.322	–0.1835
AgAu-Mg	–158805.063	–4243.214	–0.1562
AgAu-Al	–156558.980	–1996.990	–0.1606
AgAu-Ni	–158011.768	–3449.331	–0.1745

3.2.2. Mechanical properties of AgAu-M alloy

In order to reveal the mechanical properties of AgAu-M alloy, we obtained the elastic stiffness matrix of AgAu-M alloy through first principles calculations and extracted the elastic constant C_{ij}. All elastic constants are listed in Table 6. The elastic constants of all structures meet the mechanical

stability standards of the cubic crystal system and are mechanically stable. In addition, the mechanical property data of AgAu-M alloy are listed in Table 7.

Table 6. Elastic constants of AgAu-M alloy.

Alloy	C_{11} (GPa)	C_{12} (GPa)	C_{44} (GPa)
AgAu-Pd	80.07	60.66	30.36
AgAu-Pt	103.27	49.50	37.62
AgAu-Sr	93.73	59.95	29.15
AgAu-Ti	95.00	51.64	30.58
AgAu-Y	83.55	55.99	26.91
AgAu-Zn	81.00	51.50	32.26
AgAu-Be	74.26	57.31	34.67
AgAu-Cu	92.08	51.31	37.08
AgAu-Mg	97.69	53.16	37.42
AgAu-Al	78.54	50.92	27.94
AgAu-Ni	93.18	43.86	33.75

Table 7. Mechanical properties of AgAu-M alloy.

Alloy	B (GPa)	G (GPa)	E (GPa)	v	B/G	Hv (GPa)	θ_D (K)	A^U
AgAu-Pd	67.13	19.25	52.71	0.37	3.49	1.804	169.20	1.74
AgAu-Pt	67.42	32.88	84.85	0.29	2.05	4.822	221.52	0.14
AgAu-Sr	71.21	23.42	63.32	0.35	3.04	2.423	188.42	0.37
AgAu-Ti	66.09	26.64	70.46	0.32	2.48	3.345	201.24	0.14
AgAu-Y	65.18	20.57	55.84	0.36	3.17	2.109	176.40	0.56
AgAu-Zn	61.34	23.56	62.66	0.33	2.60	2.903	188.11	0.77
AgAu-Be	62.97	19.85	53.89	0.36	3.17	2.054	171.70	2.80
AgAu-Cu	64.90	29.17	76.10	0.30	2.23	4.036	209.31	0.44
AgAu-Mg	68.00	30.39	79.34	0.31	2.24	4.128	215.34	0.33
AgAu-Al	60.13	21.06	56.56	0.34	2.86	2.413	180.20	0.62
AgAu-Ni	60.30	29.76	76.68	0.29	2.03	4.555	211.83	0.12

As shown in Figure 6a, the bulk modulus is related to the average valence bond strength of the material, and the larger the bulk modulus, the greater the average valence bond strength. At the same time, the bulk modulus also reflects the degree of volume change caused by the material's resistance to external forces. Therefore, the order of alloy arrangement is arranged from small to large according to the bulk modulus B. It is obvious that AgAu-Sr alloy has the largest bulk modulus, while AgAu-Al alloy has the smallest bulk modulus. The dashed line shows the bulk modulus of $Ag_{29}Au_3$ alloy, and the microalloying elements Sr, Mg, Pt, Ti, Pd, Ti, Y, and Cu increase the bulk modulus of $Ag_{29}Au_3$ alloy. The effects of Be, Zn, Ni, and Al elements are opposite. In addition, the G and E reflect the ability of the crystalline material to resist shear strain and the material stiffness, respectively.

Poisson's ratio and B/G value are the same index, that is, reflecting the brittleness and plasticity of the crystal material. As shown in Figure 6b, the values of Poisson's ratio (v) of all alloys are greater

than 0.26, and the values of B/G are greater than 1.75. All alloys showed toughness, with the AgAu-Pd alloy had the best toughness while the AgAu-Ni alloy had the worst toughness. According to the Poisson's ratio and B/G value from high to low order: AgAu-M (Pd > Be > Y > Sr > Al > Zn > Ti > Mg > Cu > Pt > Ni). For most materials, the Poisson's ratio ranges from −1 to 0.5, and a higher Poisson's ratio generally indicates greater rigidity or stronger resistance to deformation. In ionic crystals, the Poisson's ratio is typically around 0.25. When the Poisson's ratio exceeds this value, the interatomic bonding tends to exhibit more metallic characteristics; conversely, when it is lower than 0.25, the bonding nature gradually shifts toward covalent character [44]. It can be observed that the incorporation of Pt, Ni, Mg, Cu, and Ti reduces the Poisson's ratio of the alloy to below 0.25, indicating a transition in the internal bonding character from metallic to more covalent-like bonding. This suggests stronger interatomic interactions and potentially higher hardness. The hardness of AgAu-M alloys was arranged in ascending order and plotted in Figure 6c. Compared with the hardness of $Ag_{29}Au_3$ alloy (1.785 GPa), doping with microalloying elements can increase the hardness of $Ag_{29}Au_3$ alloy to varying degrees. Among them, the microalloying element Pt has the greatest effect, making the hardness more than three times that of the original. The effect of Pd is minimal, increasing by only 2%. AgAu-M alloys are arranged in descending order of hardness: AgAu-M (Pt > Ni > Mg > Cu > Ti > Zn > Sr > Al > Y > Be > Pd).

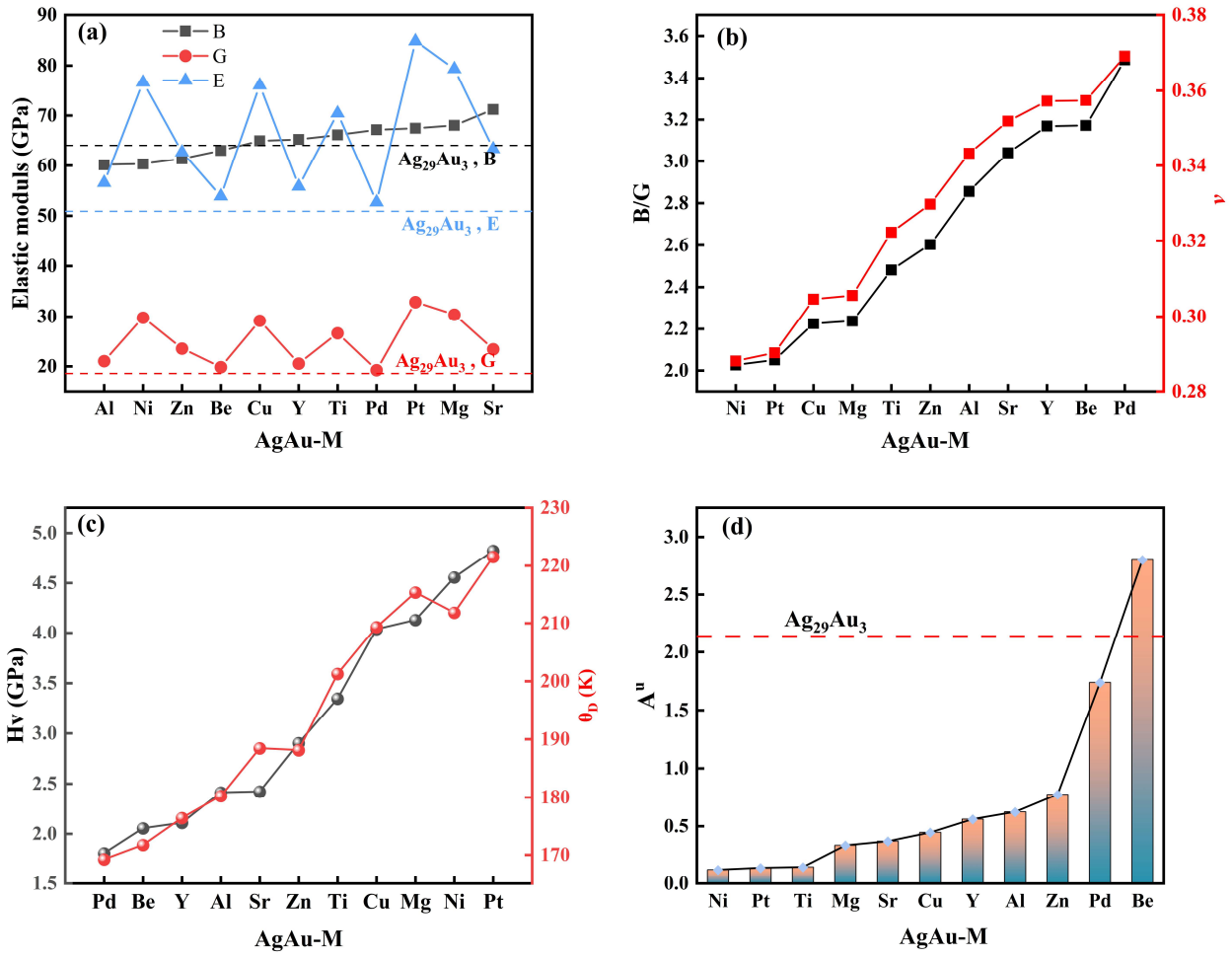

Figure 6. Mechanical properties of AgAu-M alloy. (a) Elastic modulus; (b) B/G and *ν*; (c) Hv; and (d) A^U.

The elastic anisotropy index A^U is related to the generation of microcracks inside the material. As can be seen from Figure 6d, except for Be, which increases the elastic anisotropy index, all other elements decrease A^U to varying degrees. This may be related to the significant difference in atomic radius between Be (112 pm) and Ag, Au (144 pm) [27]. The significant size difference causes significant distortion in the original lattice, introducing local stresses that are greater than those of other atoms, thereby affecting the elastic response of the alloy in different directions [45]. The AgAu-M alloy is arranged in the order of anisotropy index A^U from small to large as follows: AgAu-M (Ni < Pt < Ti < Mg < Sr < Cu < Y < Al < Zn < Pd < Be), and arrange the three-dimensional space diagrams of Young's modulus in this order. From the Figure 7, it can be seen that the deviation of the three-dimensional space diagram of Young's modulus of AgAu Ni alloy from spherical shape is small, corresponding to the smallest elastic anisotropy index A^U. The deviation of AgAu Be alloy from spherical shape is the largest, corresponding to the largest A^U value. Similar to the $Ag_{29}Au_3$ alloy, the AgAu-M alloy has low modulus values in the [001], [010], and [100] directions, and is susceptible to deformation by external forces in these directions. However, in terms of the range of scale values, trace element doping has resulted in a significant increase in the modulus values of the $Ag_{29}Au_3$ alloy in the [001], [010], and [100] directions, and there is a significant improvement in the stiffness in these three directions.

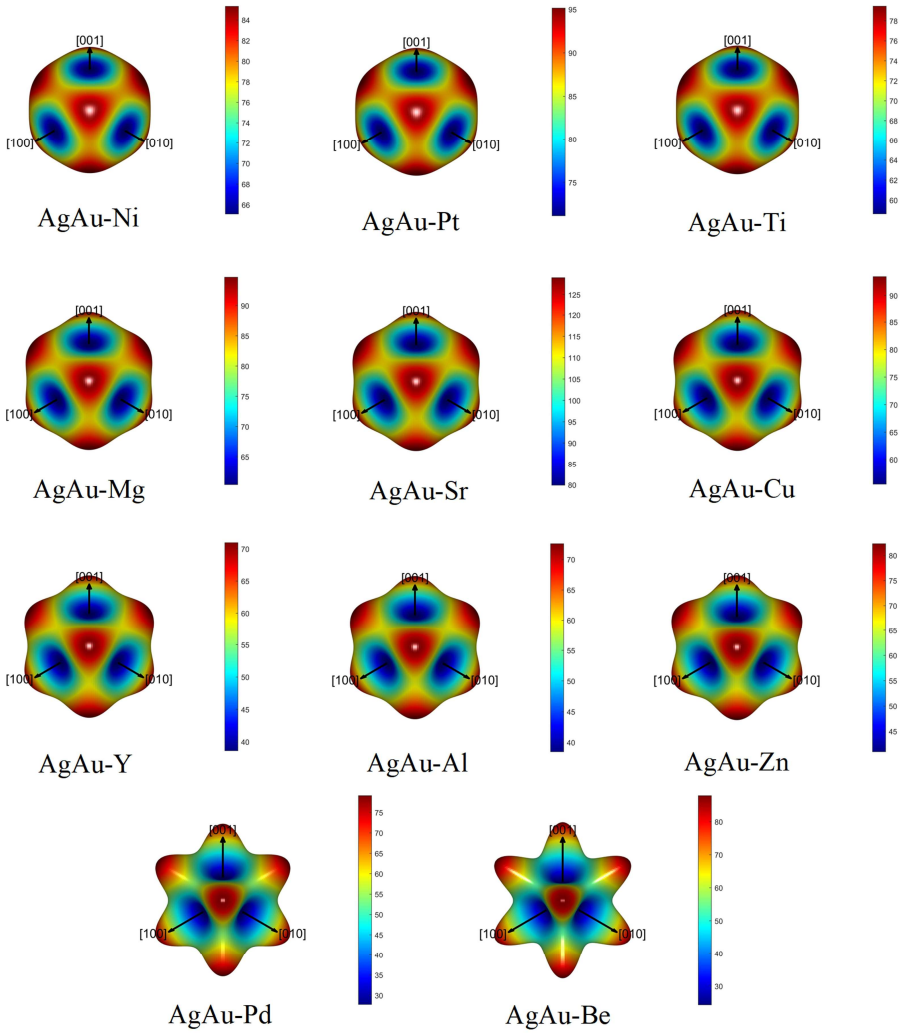

Figure 7. Three-dimensional diagrams of Young's modulus of AgAu-M alloy.

3.2.3. Electronic properties of AgAu-M alloy

In addition, we also calculated the TDOS of AgAu-M alloy, as shown in Figure 8. Figure 8a shows the TDOS of AgAu-M alloy and $Ag_{29}Au_3$ alloy in the range of −0.05~0.05 eV, while Figure 8b,c are two enlarged partial views of Figure 8a. The results show that the incorporation of microalloying elements Pt, Y, Sr, Be, Ti, and Pd enhances the TDOS of $Ag_{29}Au_3$ alloy at E_f, indicating that more electrons that should be located below the Fermi level have crossed the Fermi level to become conductive electrons, thereby improving the electronic conductivity of the alloy. However, the microalloying elements Cu, Zn, Ni, Mg, and Al have opposite effects on the $Ag_{29}Au_3$ alloy. Figure 8d shows the TDOS in the energy range of −10~10 eV. It can be seen that all alloys form bonds in the range of −7~10 eV, with the difference being that AgAu-Al alloy has a density of states peak in the range of −8~−7 eV, and AgAu-Mg alloy also has a density of states peak in the range of −9~−8 eV. In addition, there exists an intrinsic correlation between the electronic structure and mechanical performance of the alloy system. After microalloying, a noticeable redistribution of the density of states near the E_f is observed, accompanied by enhanced d orbital hybridization and increased electron cloud overlap. These modifications in the electronic structure are consistent with the increasing trends of the elastic constants C_{11} and C_{44}, indicating that microalloying strengthens the directional bonding between atoms and thereby improves the resistance to shear deformation. According to the Pugh criterion (B/G ratio), the ductility of a material is closely related to its bonding characteristics. Enhanced d-orbital hybridization and stronger bonding directionality generally lead to a higher shear modulus, whereas increased electron delocalization enhances metallic bonding and thus improves ductility. Combined analysis of the density of states at the Fermi level and the B/G values shows that doping elements, such as Pd, Be, Sr, and Y, significantly increase the density of states at E_f, thereby enhancing the metallic character of the alloy. This enhanced metallicity implies improved ductility, which is consistent with the observed increase in B/G values. These results demonstrate that electronic structure regulation via microalloying is an effective approach for improving the ductility of the alloy [44].

Overall, microalloying modifies the local electronic environment and orbital hybridization behavior, thereby strengthening the bonding interactions between alloying elements and the matrix. This leads to a downward shift of bonding states toward lower energy levels and a redistribution of electronic states near the Fermi level, ultimately enhancing bonding strength and structural stability. The increased electron delocalization correlates with the improvement in elastic moduli, while the optimization of the B/G ratio reflects enhanced ductility. Meanwhile, the stabilization of deeper energy levels contributes to improved thermal stability. Therefore, microalloying enables the synergistic optimization of strength and ductility, providing electronic-structure-based theoretical support for the potential application of these materials in high-strength conductive components and high-temperature structural systems.

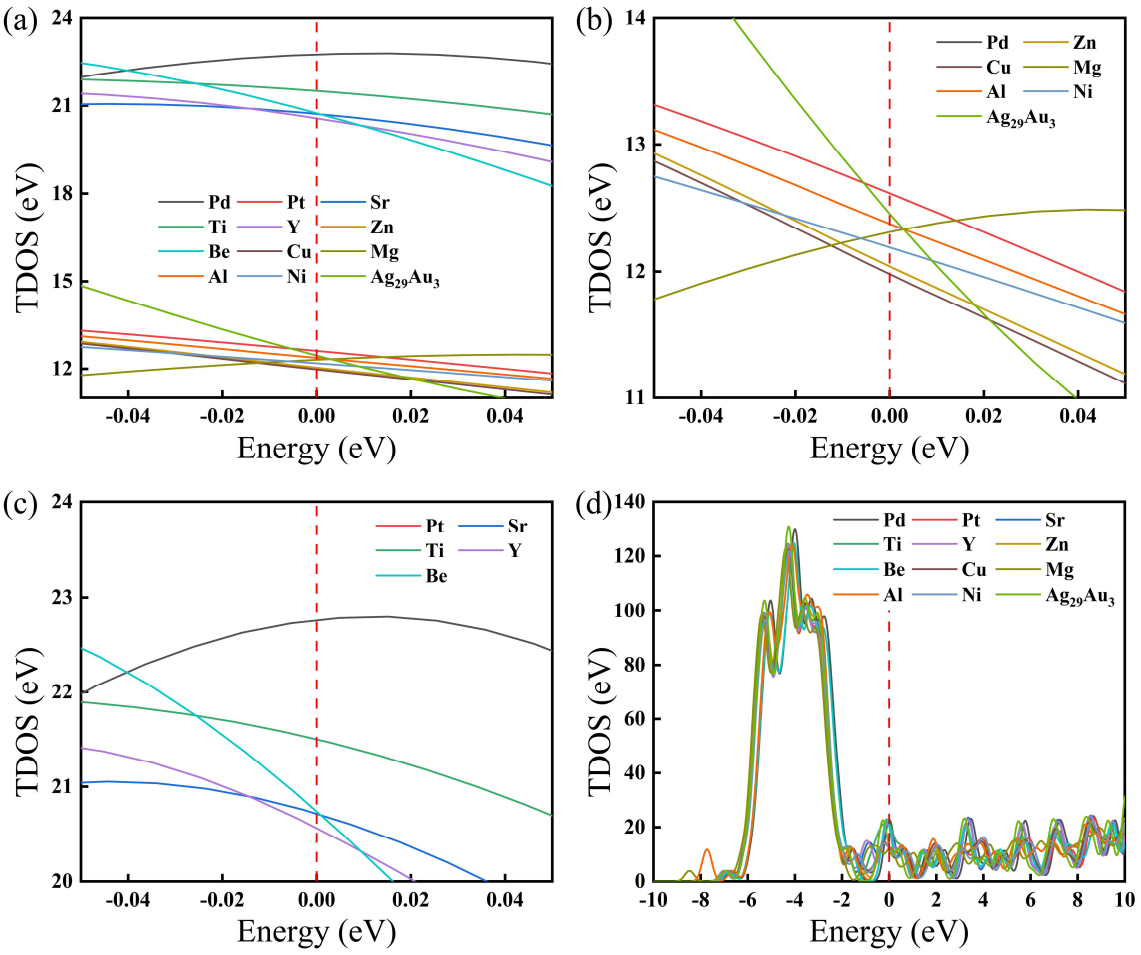

Figure 8. TDOS of AgAu-M alloy: (a) TDOS in the energy range of –0.05~0.05 eV; (b) and (c) partial enlarged image of (a); (d) TDOS in the energy range of –10~10 eV.

3.3. Experimental results

Figure 9a shows the XRD pattern of the Ag-16wt%Au-0.5wt%Al alloy. After analysis and comparison, the peaks are consistent with the PDF cards of Ag, Au, and AlAu, which means the room-temperature microstructure of the alloy is mainly composed of Ag, Au, and AlAu. Figure 9b shows a comparison between the calculated hardness values and the experimentally measured hardness values. It is obvious that the calculated hardness is slightly higher than the experimental value. This is because the first-principles calculations simulate a perfect solid solution of Ag doping Au and Al, and the solid solution strengthening effect is significant. Intermediate phases, defects, and cracks may exist in actual alloys, which will have a certain impact on the hardness. To clarify the distribution of elements and intermediate phases, this paper conducted an EDS analysis of the alloy. Figure 9c shows the EDS area scan results of the alloy. It can be seen that Ag elements occupy a large number of positions in the form of a matrix, and Au and Al elements are mainly distributed between the Ag matrix. According to the XRD results, it can be speculated that Au and Al appear in the form of the AlAu intermetallic phase. In addition, a large amount of Au element is dissolved in the Ag matrix, while a small amount of Al is dissolved in the Ag matrix. Figure 9d shows the spot scan results of the alloy. The proportion of Ag elements at points a and b exceeds 88wt%, indicating that the gray areas are the

Ag matrix, and at the same time, a certain amount of Au and Al are solid-soluted in it, which is consistent with the area scan results. Furthermore, the atomic percentage of Al and Ag is close to 1:2, suggesting that a trace amount of $AlAu_2$ may have precipitated within the Ag matrix. However, due to its extremely low content, no corresponding diffraction peaks were detected by XRD. At Points c and d, the atomic percentages of Au and Al increase while the Ag content decreases. The atomic ratio of Au to Al is close to 1:1, suggesting that the AlAu phase is distributed in the white regions of the image. This area is likely a mixture of the AlAu phase and the AgAu solid solution. Therefore, solid solution strengthening is the main factor that improves the hardness of AgAu alloys.

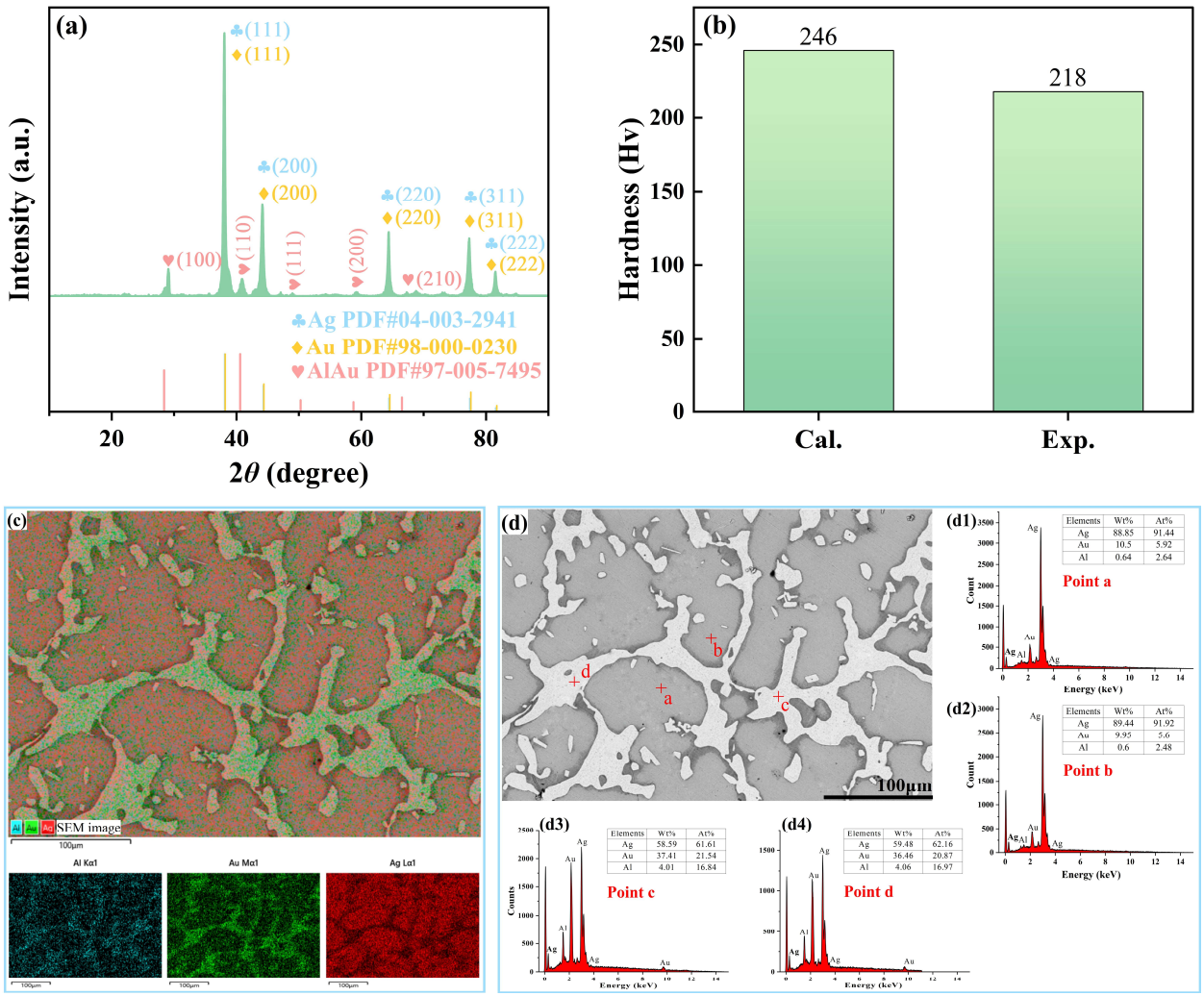

Figure 9. (a) XRD pattern of Ag-16wt%Au-0.5wt%Al alloy; (b) calculated hardness and experimental hardness of Ag-16wt%Au-0.5wt%Al alloy; (c) EDS area scan of Ag-16wt%Au-0.5wt%Al alloy; (d) EDS spot scan of Ag-16wt%Au-0.5wt%Al alloy.

Based on the three binary marginal phase diagrams of Ag-Au, Ag-Al and Au-Al and their binary thermodynamic databases, Deng et al. [46] extrapolated the Ag-Au-Al ternary phase diagram, and its isothermal section at 25 ℃ consists of 14 regions. The composition of the alloy sample in this paper is located within the [Fcc (i.e., Ag(Au, Al) solid solution) + AlAu + $AlAu_2$)] phase region. The room temperature microstructure of this phase region consists of an Ag(Au, Al) solid solution, AlAu, and

$AlAu_2$, which is consistent with our analysis results and mutually corroborates with each other. In addition, the formation of new phases involves many factors and processes, including but not limited to diffusion, nucleation, growth, and the interfacial energy between new and old phases. Here, we only use the formation enthalpy as an indicator to simply illustrate the difficulty of forming AlAu and $AlAu_2$. This is a poor consideration, but the precipitation relationship between AlAu and $AlAu_2$ in the Ag(Au, Al) solid solution still requires more experimental support. As shown in Table 8, the formation enthalpy of AlAu is smaller, which means that under the same conditions and environment, it is easier to produce the AlAu phase. Therefore, during the cooling process, the Ag(Au, Al) solid solution transformed into more AlAu phase. In the future, advanced transmission electron microscopy (TEM) techniques, such as high-resolution TEM (HRTEM) and selected-area electron diffraction (SAED), could be employed to gain a deeper understanding of the phase structures.

Table 8. Formation enthalpy for AlAu and $AlAu_2$.

Phase	E_{total} (eV/atom)	Generate enthalpy (eV/atom)
AlAu	–3885.371	–0.488
$AlAu_2$	–3770.903	–0.379

4. Conclusions

First-principles calculations show that all $Ag_{32-x}Au_x$ alloys have thermodynamic and mechanical stability and exhibit ductility. All AgAu-M alloys meet the requirements for thermodynamic and mechanical stability, and still have a certain degree of toughness. The microalloying elements increase the hardness of the $Ag_{29}Au_3$ alloy to varying degrees, with the most obvious effect being the Pt element, which makes the hardness more than three times the original. With the exception of Be, the other micro-alloying elements all reduced the elastic anisotropy index of the $Ag_{29}Au_3$ alloy to varying degrees, with Ni having the most significant effect. Pt, Y, Sr, Be, Ti, and Pd increased the total electronic density of states of the $Ag_{29}Au_3$ alloy at Ef, while Cu, Zn, Ni, Mg, and Al did the opposite. The DOS show that all alloys have metallic properties and that $Ag_{29}Au_3$ alloy has the lowest DOS value at the E_f, as well as more stable properties.

An Ag-16wt%Au-0.5wt%Al alloy was prepared experimentally, and the XRD results showed that the alloy has Ag and Au phases and that an AlAu phase was formed. Compared with the calculated hardness value, the experimental hardness value is slightly lower than the calculated value. The EDS area scan results prove that the alloy matrix is an Ag(Au, Al) solid solution, and the intermediate phase AlAu is distributed in the matrix. EDS spot scan analysis found that a trace amount of $AlAu_2$ intermetallic phase may also be mixed in the Ag(Au, Al) solid solution, and the ratio of Al to Au in the white area is close to 1:1, which also proves the formation of the AlAu phase. This study provides some reference value for the research on improving the performance of the AgAu system by doping with micro-alloying elements.

Use of AI tools declaration

The authors declare they have not used Artificial Intelligence (AI) tools in the creation of this article.

Acknowledgements

This work was financially supported by Scientific and Technological Project of Yunnan Precious Metals Laboratory (YPML-20240502011).

Author contributions

Lisen Huang: investigation, data curation, writing-original draft; Kun Zhu: investigation, formal analysis; Jianying Yang: methodology, writing-review and editing; Junjie Feng: formal analysis, data curation; Hui Xiong: methodology; Rong Jiang; visualization; Xiaolong Zhou: funding acquisition, software, writing-review and editing, supervision.

Conflict of interest

The authors declare no conflict of interest.

References

1. Cao J, Fan J, Gao W (2016) Effect of Ag-4Pd alloy bonding wire properties and structure on bond strengths and reliability. 2016 International Conference on Electronics Packaging (ICEP), Hokkaido, Japan, 502–507. https://doi.org/10.1109/ICEP.2016.7486878
2. Hailu A, Shaw SK (2020) Implications of surface strain for enhanced carbon dioxide reduction on copper-silver alloys. *J Electrochem Soc* 167: 126509. https://doi.org/10.1149/1945-7111/abaf74
3. Park J, Lee J, Park S, et al. (2016) Development of hybrid process for double-side flexible printed circuit boards using roll-to-roll gravure printing, via-hole printing, and electroless plating. *Int J Adv Manuf Technol* 82: 1921–1931. https://doi.org/10.1007/s00170-015-7507-2
4. Zhou W, Apkarian R, Wang Z, et al. (2006) Fundamentals of scanning electron microscopy (SEM), In: Zhou W, Wang Z, *Scanning Microscopy for Nanotechnology*, New York: Springer, 1–40. https://doi.org/10.1007/978-0-387-39620-0_1
5. Shi Z, Zhang L, Ma Y, et al. (2022) Kinetics and mechanism of the sulfurization behavior of silver conductive material in automobile industry. *Rare Met* 41: 37–44. https://doi.org/10.1007/s12598-021-01803-3
6. Bacon R, Smith CS (1956) Single crystal elastic constants of silver and silver alloys. *Acta Metall* 4: 337–341. https://doi.org/10.1016/0001-6160(56)90021-9
7. Kuo B, Tsai D, Huang Y, et al. (2019) Effect of alloying Au on the microstructural, mechanical and electrical properties of Ag-based alloy wires. *J Mater Sci Mater Electron* 30: 9396–9409. https://doi.org/10.1007/s10854-019-01270-8
8. Nakamichi I (1996) Electrical resistivity and grain boundaries in metals. *Mater Sci Forum* 207–209: 47–58. https://doi.org/10.4028/www.scientific.net/MSF.207-209.47
9. Tseng Y, Hung F, Lui T, et al. (2015) Effect of annealing on the microstructure and bonding interface properties of Ag–2Pd alloy wire. *Microelectron Reliab* 55: 1256–1261. https://doi.org/10.1016/j.microrel.2015.05.012

10. Jiang C, Sordelet DJ, Gleeson B (2006) Effects of Pt on the elastic properties of B2 NiAl: A combined first-principles and experimental study. *Acta Mater* 54: 2361–2369. https://doi.org/10.1016/j.actamat.2006.01.010
11. Hu J, Xie M, Chen Y, et al. (2022) Thermodynamic reassessment of Au-Pt-Sn system. *Mater Res Express* 9: 016507. https://doi.org/10.1088/2053-1591/ac475f
12. Delczeg-Czirjak EK, Delczeg L, Vitos L, et al. (2015) Monovacancy formation energies and fermi surface topological transitions in Pd-Ag alloys. *Phys Rev B* 92: 224107. https://doi.org/10.1103/PhysRevB.92.224107
13. Semidey-Flecha L, Ling C, Sholl DS (2010) Detailed first-principles models of hydrogen permeation through PdCu-based ternary alloys. *J Membr Sci* 362: 384–392. https://doi.org/10.1016/j.memsci.2010.06.063
14. Gong H (2010) Electronic structures and related properties of Ag-Au bulks and surfaces. *Mater Chem Phys* 123: 326–330. https://doi.org/10.1016/j.matchemphys.2010.04.024
15. Han X, Liu M, Zhou X (2023) Calculation of mechanical properties, electronic properties, and thermodynamic properties of AuAl crystal: First-principles calculation. *Cryst Res Technol* 58: 2300061. https://doi.org/10.1002/crat.202300061
16. Yi Z, Hu J, Wen D, et al. (2023) Impact of alloying elements on generalized stacking fault energy and twinning of Ag-based alloys. *Phys B* 670: 415368. https://doi.org/10.1016/j.physb.2023.415368
17. Bellaiche L, Vanderbilt D (2000) Virtual crystal approximation revisited: application to dielectric and piezoelectric properties of perovskites. *Phys Rev B* 61: 7877–7882. https://doi.org/10.1103/PhysRevB.61.7877
18. Raphel A, Vivekanandhan P, Rajasekaran AK, et al. (2022) Tuning figure of merit in Na doped nanocrystalline PbSnTeSe high entropy alloy via band engineering. *Mater Sci Semicond Process* 138: 106270. https://doi.org/10.1016/j.mssp.2021.106270
19. Hashimoto Y, Seniutinas G, Balcytis A, et al. (2016) Au-Ag-Cu nano-alloys: Tailoring of permittivity. *Sci Rep* 6: 25010. https://doi.org/10.1038/srep25010
20. Levy M (1979) Universal variational functionals of electron densities, first-order density matrices, and natural spin-orbitals and solution of the v-representability problem. *Proc Natl Acad Sci USA* 76: 6062–6065. https://doi.org/10.1073/pnas.76.12.6062
21. Clark SJ, Segall MD, Pickard CJ, et al. (2005) First principles methods using CASTEP. *Z Kristall* 220: 567–570. https://doi.org/10.1524/zkri.220.5.567.65075
22. Perdew JP, Burke K, Ernzerhof M (1996) Generalized gradient approximation made simple. *Phys Rev Lett* 77: 3865–3868. https://doi.org/10.1103/PhysRevLett.77.3865
23. Lejaeghere K, Van Speybroeck V, Van Oost G, et al. (2014) Error estimates for solid-state density-functional theory predictions: An overview by means of the ground-state elemental crystals. *Crit Rev Solid State Mat Sci* 39: 1–24. https://doi.org/10.1080/10408436.2013.772503
24. Kresse G, Furthmüller J (1996) Efficient iterative schemes for *ab initio* total-energy calculations using a plane-wave basis set. *Phys Rev B* 54: 11169–11186. https://doi.org/10.1103/PhysRevB.54.11169
25. Pfrommer BG, Côté M, Louie SG, et al. (1997) Relaxation of crystals with the quasi-newton method. *J Comput Phys* 131: 233–240. https://doi.org/10.1006/jcph.1996.5612
26. Owen EA, Williams GI (1954) A low-temperature X-ray camera. *J Sci Instrum* 31: 49. https://doi.org/10.1088/0950-7671/31/2/305

27. Warlimont H, Martienssen W (2018) *Springer Handbook of Materials Data*, Cham: Springer International Publishing. https://doi.org/10.1007/978-3-319-69743-7
28. Yang S, Liu M, Gan G, et al. (2023) First-principles study on X (Co, In, Ni, pd, Ge, Ca) doping on the structural stability and mechanical properties of AlCu. *Cryst Res Technol* 58: 2300142. https://doi.org/10.1002/crat.202300142
29. Mouhat F, Coudert FX (2014) Necessary and sufficient elastic stability conditions in various crystal systems. *Phys Rev B* 90: 224104. https://doi.org/10.1103/PhysRevB.90.224104
30. Hill R (1952) The elastic behaviour of a crystalline aggregate. *Proc Phys Soc A* 65: 349. https://doi.org/10.1088/0370-1298/65/5/307
31. Chen W, Cheng H, Yu C (2016) The mechanical, thermodynamic, and electronic properties of cubic Au_4Al crystal via first-principles calculations. *J Alloy Compd* 689: 857–864. https://doi.org/10.1016/j.jallcom.2016.08.050
32. Liu Q, Zhang N, Liu F, et al. (2014) Structural, electronic, optical, elastic properties and born effective charges of monoclinic HfO_2 from first-principles calculations. *Chinese Phys B* 23: 47101. https://doi.org/10.1088/1674-1056/23/4/047101
33. Teter DM (1998) Computational alchemy: The search for new superhard materials. *MRS Bull* 23: 22–27. https://doi.org/10.1557/S0883769400031420
34. Tian Y, Xu B, Zhao Z (2012) Microscopic theory of hardness and design of novel superhard crystals. *Int J Refract Met Hard Mat* 33: 93–106. https://doi.org/10.1016/j.ijrmhm.2012.02.021
35. Chen XQ, Niu H, Li D, et al. (2011) Modeling hardness of polycrystalline materials and bulk metallic glasses. *Intermetallics* 19: 1275–1281. https://doi.org/10.1016/j.intermet.2011.03.026
36. Yang W, Zhang X, Wang F (2023) The elastic anisotropy, electronic and optical properties of $Bi_4Si_3O_{12}$, Bi_2SiO_5, $Bi_{12}SiO_{20}$ and $Bi_2Si_3O_9$ crystals from first-principles calculations. *Chem Phys Lett* 814: 140323. https://doi.org/10.1016/j.cplett.2023.140323
37. Anderson OL (1963) A simplified method for calculating the debye temperature from elastic constants. *J Phys Chem Solids* 24: 909–917. https://doi.org/10.1016/0022-3697(63)90067-2
38. Nielsen OH, Martin RM (1985) Quantum-mechanical theory of stress and force. *Phys Rev B* 32: 3780–3791. https://doi.org/10.1103/PhysRevB.32.3780
39. Ranganathan SI, Ostoja-Starzewski M (2008) Universal elastic anisotropy index. *Phys Rev Lett* 101: 55504. https://doi.org/10.1103/PhysRevLett.101.055504
40. Anderson TL (2017) *Fracture Mechanics: Fundamentals and Applications*, 4 Eds., Boca Raton: CRC Press, 25–65. https://doi.org/10.1201/9781315370293
41. Kittel C (2022) Introduction to solid state physics, In: Olaf Stenzel, *Light–Matter Interaction*, Hoboken: Springer, 397–425. https://doi.org/10.1007/978-3-030-87144-4_16
42. Peng G, Gan X, Li Z, et al. (2018) First-principles study of the $(Cu_xNi_{1-x})_3Sn$ precipitations with different structures in Cu–Ni–Sn alloys. *Chinese Phys B* 27: 086302. https://doi.org/10.1088/1674-1056/27/8/086302
43. Zhang C, Yan M, You Y, et al. (2014) Stability and properties of alloyed ε-$(Fe_{1-x}M_x)_3N$ nitrides (M = Cr, Ni, Mo, V, Co, Nb, Mn, Ti and Cu): A first-principles calculations. *J Alloys Compd* 615: 854–862. https://doi.org/10.1016/j.jallcom.2014.07.069
44. Song Y, Wang G, Ni J, et al. (2024) First-principles study on the structural, mechanical and thermodynamic properties of Cu-Cr-Zr alloy. *Phys B* 685: 416029. https://doi.org/10.1016/j.physb.2024.416029

45. Jiang F, Yu H, Hu Q, et al. (2020) Effect of alloying elements on lattice misfit and elasticities of Ni-based single crystal superalloys by first-principle calculations. *Solid State Commun* 310: 113852. https://doi.org/10.1016/j.ssc.2020.113852
46. Deng L, Wang X, Zhou X, et al. (2024) Thermodynamic optimization and calculation of the phase diagrams of Au-Ag-Al system. *Precious Met* 45: 11–18. https://doi.org/10.3969/j.issn.1004-0676.2024.02.002

AIMS Press